CONTENTS

Note S1: optical confinement of the superfluid - The prove the effectiveness of the optical confinement by means of an out of resonance ring, we looked at the time evolution of the superfluid with the aid of a streak camera. Figure S1 shows the evolution of a central horizontal slice of the condensate without (left) and with boundaries (right). In the latter the dynamics of the system can be followed for a much longer time, whereas without any type of confinement the superfluid quickly expands.

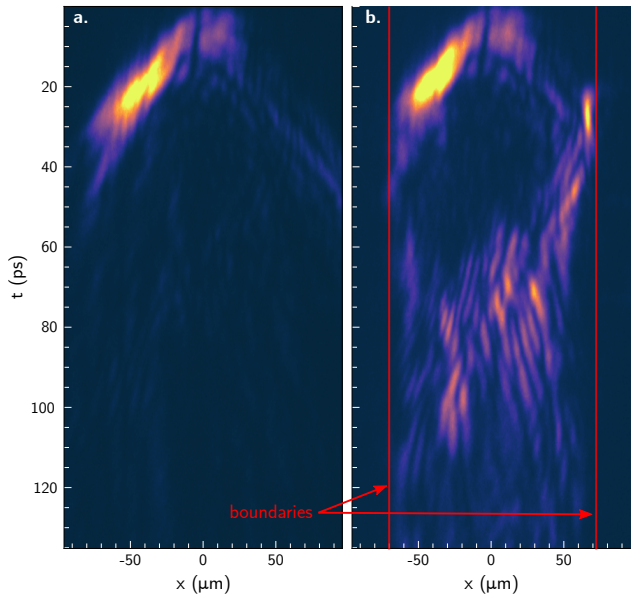

FIG. S1. Streak camera images of the central slice of the superfluid without (a) and with (b) the optical confinement. The red vertical lines represent the size of the barrier.

Note S2: experimental setup - The schematic representation of the experimental setup, with a complete description of the optics and the lines, is shown in Fig. S2. The pulsed laser (2 ps, 80 MHz) is used to quasi-resonantly excite the system (beam 1. in Fig. S2) at ~ 772.9 nm for the H case and at ~ 773.4 nm for L. The trapping, as discussed in the main text, is made with an out of resonance CW laser at ~ 730 nm. To shape the beam as a ring we employed a phase-only SLM with a Bessel pattern, working with a diffraction grating to carry on only the modulated part of the beam.

The signal and the reference beam form an angle (not visible in Fig. S2), for an easier separation of the information contained in the interferograms that we measure.

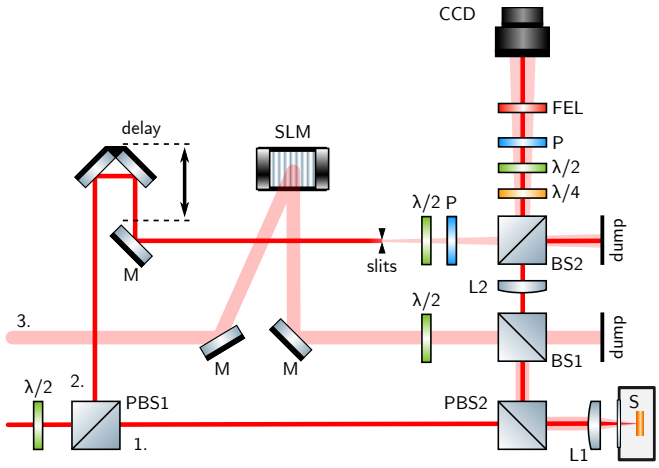

FIG. S2. A schematic representation of the experiment. The pulsed laser beam is split in two (1., 2.) by a polarizing beam splitter (PBS1), coupled with a half-waveplate to tune the power in each arm. The first beam (1.) arrives focused on the sample (S), with a linear polarization, through a 5 cm camera objective (L1). The photoluminescence from the sample is collected by a second polarizing beam splitter (PBS2) which also serves as a first filter for the laser beam. The second beam (2.) hits a retroreflector mounted on a moving stage, which allows for fine adjustments of its optical path length. This beam then passes through an iris to create a spherical light source so that, after its propagation, we get a reference beam with a relatively flat phase. The two beams (1., 2.) are then put back together at a beam splitter (BS2). A half-waveplate and a polarizer ensure that the reference has the same polarization as the emission. A Bessel phase is imprinted on a CW laser (3.) with a spatial light modulator (SLM); this beam enters the sample from a beam splitter (BS1) placed in the detection line and a half-waveplate is used to tune the power that passes through PBS2. The camera objective (L1) Fourier transforms this beam into a ring, that is then used to confine the superfluid. The image from the sample is reconstructed on the CCD with a 100 cm lens (L2), after passing through a set of waveplates and a polarizer to extinguish the resonant laser and a long-pass filter to block the non-resonant one. The beam sizes and the length of the lines are not to scale, and unnecessary reflections from the beam splitters (BS) have been omitted.

Note S3: Helmholtz decomposition of the velocity - To disentangle the velocity into its incompressible and compressible parts, we adopt the Helmholtz decomposition for vector fields. Given $\boldsymbol{v}(\boldsymbol{x})$, we can write it as the sum of a potential and a divergence-free

contribution: $\boldsymbol{v}(\boldsymbol{x}) = \nabla\phi(\boldsymbol{x}) + \nabla \times \boldsymbol{A}(\boldsymbol{x})$, where ϕ and $\boldsymbol{A}$ are a scalar and a vector field, respectively. In the Fourier space, the decomposition has a straight-forward implementation. Indeed, given the vector field in real space $\boldsymbol{v}(\boldsymbol{x})$:

$$\boldsymbol{V}(\boldsymbol{k}) = \frac{1}{2\pi} \int e^{-i\boldsymbol{k}\cdot\boldsymbol{x}} \boldsymbol{v}(\boldsymbol{x}) d\mathcal{S}_x \,,$$

which can be decomposed as

$$\boldsymbol{V}(\boldsymbol{k}) = i\boldsymbol{k} V_\phi(\boldsymbol{k}) + i\boldsymbol{k} \times \boldsymbol{V}_{\boldsymbol{A}}(\boldsymbol{k}) \tag{S1}$$

where we used the scalar and vector fields:

$$V_\phi(\boldsymbol{k}) = -i \, \frac{\boldsymbol{k} \cdot \boldsymbol{V}(\boldsymbol{k})}{||\boldsymbol{k}||^2}$$

$$\boldsymbol{V}_{\boldsymbol{A}}(\boldsymbol{k}) = i \, \frac{\boldsymbol{k} \times \boldsymbol{V}(\boldsymbol{k})}{||\boldsymbol{k}||^2}.$$

Once evaluated these in Fourier space, back to real space we finally have:

$$\nabla\phi(\boldsymbol{x}) = \int e^{i\boldsymbol{k}\cdot\boldsymbol{x}} \, i\boldsymbol{k} V_\phi(\boldsymbol{k}) d\mathcal{S}_k$$

$$\nabla \times \boldsymbol{A}(\boldsymbol{x}) = \int e^{i\boldsymbol{k}\cdot\boldsymbol{x}} \, i\boldsymbol{k} \times \boldsymbol{V}_{\boldsymbol{A}}(\boldsymbol{k}) d\mathcal{S}_k$$

which are the potential and divergence-free components of the velocity field, respectively.

Note S4: kinetic energy decomposition - At any given time of the temporal evolution, the total energy of the quantum fluid can be written as the sum of hydrodynamic kinetic, quantum pressure, potential, and interaction contributions [1, 2]:

$$E_{\rm tot} = E_{\rm kin} + E_{\rm q} + E_{\rm V} + E_{\rm I} \,, \tag{S2}$$

where

$$\begin{aligned}
E_{\rm kin} &= m/2 \int n(\boldsymbol{x},t) |\boldsymbol{v}(\boldsymbol{x},t)|^2 d\mathcal{S}_x \,, \\
E_{\rm q} &= \hbar^2/(2m) \int |\sqrt{n(\boldsymbol{x},t)}|^2 d\mathcal{S}_x \,, \\
E_{\rm V} &= \int n(\boldsymbol{x},t) V(\boldsymbol{x},t) d\mathcal{S}_x \,, \\
E_{\rm I} &= g/2 \int n(\boldsymbol{x},t)^2 d\mathcal{S}_x.
\end{aligned}$$

Clearly in our case, this is not conserved in time, since we loose polaritons.

The hydrodinamics kinetic (from now on, simply kinetic) energy $E_{\rm kin} = m/2 \int n(\boldsymbol{x},t)|\boldsymbol{v}(\boldsymbol{x},t)|^2 d\mathcal{S}_x$ can be further decomposed in *incompressible* and *compressible* components, which are attributed to the kinetic energy of quantum vortices and of the sound excitation, respectively. Following Refs. [2–4] we define a density-weighted velocity field $\boldsymbol{u}(\boldsymbol{x},t) = \sqrt{n(\boldsymbol{x},t)}\boldsymbol{v}(\boldsymbol{x},t)$ and decompose it as:

$$\boldsymbol{u}(\boldsymbol{x},t) = \boldsymbol{u}^{\rm inc}(\boldsymbol{x},t) + \boldsymbol{u}^{\rm comp}(\boldsymbol{x},t), \tag{S3}$$

where the incompressible and compressible field satisfies $\boldsymbol{\nabla}\cdot\boldsymbol{u}^{\rm inc} = 0$ and $\boldsymbol{\nabla}\times\boldsymbol{u}^{\rm com} = 0$, respectively. In Fourier space, the total incompressible kinetic energy reads as

$$E_{\rm kin}^{\rm inc} = \frac{m}{2}\sum_{i=x,y}\int |U_i^{\rm inc}(\boldsymbol{k})|^2 d\mathcal{S}_k, \tag{S4}$$

with

$$U_i^{\rm inc}(\boldsymbol{k}) = \frac{1}{2\pi}\int e^{-i\boldsymbol{k}\cdot\boldsymbol{x}} u_i^{\rm inc}(\boldsymbol{x})\, d\mathcal{S}_x\,. \tag{S5}$$

Finally, since the system geometry is isotropic we can simply consider the longitudinal energy spectrum $E_{\rm kin}(k)$ (where we have dropped the incompressible label for simplicity), which is obtained by integrating over the azimuthal angle as

$$E_{\rm kin}(k) = \frac{m}{2}k\sum_{i=x,y}\int_\Omega d\Omega_k |U_i^{\rm inc}(\boldsymbol{k})|^2\,. \tag{S6}$$

Note S5: previous configurations - Several configurations were tested before the one used in the main text, all of which employed a second SLM to imprint in a controllable any desired vortex distribution as initial configuration on a flat polariton superfluid.

Free expansion (Fig. S3a): without the trapping potential, polaritons are free to expand indefinitely and the inter-vortex distance increases with time. In this configuration, vortex-vortex interactions are too weak and the correlation function C decreases from C=-0.75 at t=0 towards C=-1 at later times.

High vortex density imprinted externally (Fig. S3b).: to increase the vortex-vortex interaction, a random distribution of a large number of vortices and antivortices with C=0 can be imprinted in the pulsed beam directly by the SLM. In this case, the condensate fills the whole trap since the beginning, without initial expansion. However, using this technique to inject a random distribution of vortices in a homogeneous polariton fluid is not effective:

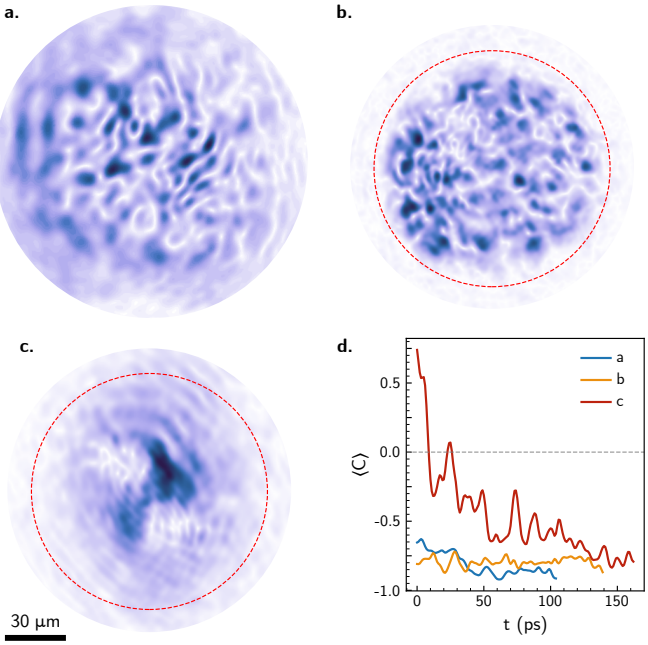

FIG. S3. Snapshots of the configurations used before the successful one described in the paper. (**a**) Without a trapping potential the superfluid expands way faster than the average speed of vortices, causing an overall increase of the mean distances. (**b**) Confining the superfluid in a circular potential and increasing the polariton density stabilised the number of vortices in time but nucleation (and annihilation) is still the predominant process. (**c**) Starting from two clusters the superfluid quickly becomes inhomogeneous and dipoles start to appear. (**d**) Value of the first order correlation function for the configurations in a, b, and c.

even if the number of vortices is more or less constant over time, we observe that the value of the first order correlation function is negative from the very beginning of the polariton dynamics. Indeed, vortices and antivortices just annihilate before reaching the sample during propagation in the linear medium (air), creating a very inhomogeneous condensate with a large number of dipoles and C decreasing quickly with time towards C=-1.

Externally imprinted clusters (Fig. S3c): we inject a flat polariton fluid with two clusters of vortices with positive and negative circulation, respectively, corresponding to the configuration with C=1. Also in this case, the polariton fluid is injected with the same size as the trap, without initial expansion. We observe the breaking of the cluster structure in time, accompanied with the nucleation of a large number of dipoles in the low-density regions of the condensate, quickly bringing the correlation towards C=-1.

Fig. S3d shows the temporal evolution of the first order correlation function in the three cases, where C is always decreasing towards C=-1. Indeed, we find that the collision of the expanding polariton fluid against the potential barrier is the best strategy to induce the hydrodynamic nucleation of a large number of vortices and antivortices in this system, avoiding the annihilation of vortices of opposite sign that occurs when external imprinting techniques and propagation through linear materials are used. Moreover, the formation of sound waves enables the injection of incompressible kinetic energy into the vortex distribution, as shown in Fig. 3a of the main text.

Note S6: low energy vortex distribution - We report in Fig. S4 the three vortex species fractions, namely dipoles (ρ_d), clusters (ρ_c) and free vortices (ρ_f), together with the total number of vortices, for the L case. Contrary to what is show in Fig. 3b of the main text we can observe in this case slower dynamics of the superfluid, with the formation of the vortices due to the backflow taking place at a later time ($\sim$ 10 ps). The three populations remain approximately constant throughout the evolution, with the dipoles being the highest fraction at all times.

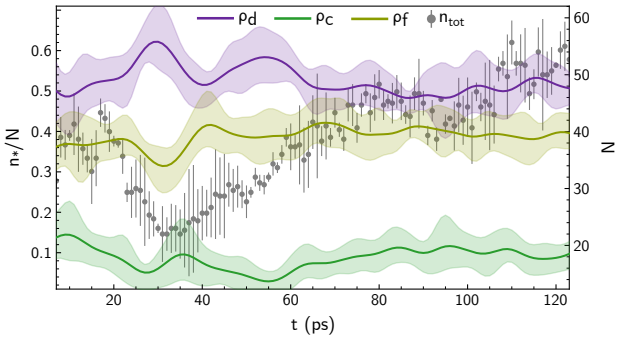

FIG. S4. Mean values (over four realisations) of the fractions of dipoles (ρ_d, purple line), clusters (ρ_c, green line) and free vortices (ρ_f, yellow line), together with their respective standard deviations, for the low energy configuration. The total number of vortices in time is shown by the gray scatter plot as a mean of the same configurations $\pm$ SD.

Note S7: turbulent estimates - To find the signature of turbulent behaviour, the simplest observable is a two-point statistical object. In the section above, we have defined the isotropic (or longitudinal) energy spectrum $E_{\rm kin}(k) = m\pi k\langle|\mathbf{U}^{\rm inc}(k)|^2\rangle$, from which the total incompressible kinetic energy can be obtained as the sum over all $k = |\mathbf{k}|$, $E_{\rm kin} =$

$\int E_{\rm kin}(k)\ dk$.

Here we want to dimensionally estimate the characteristic time-scales of the turbulent inverse energy cascade [5], and see if these are compatible with our experimental measurements. To do that, the starting point is the observation that $E_{\rm kin}(k) \sim k^{-5/3}$ in some range of wavenumbers, that in our experiments is $k_c < k < k_\xi$, where k_c is the inverse of to the typical cluster scale l_c, and k_ξ is the inverse of the healing length ξ. The characteristic times τ_{lc} of the clusters at scale $l_c \simeq 1/k_c$ in the turbulent inverse cascade obeys the scaling law $\tau_{lc} \simeq l_c^{2/3}$ (or equivalently the characteristic frequencies of cluster of size k obey $\omega_k \simeq k^{2/3}$ for $k_c < k < k_\xi$).

To make the scaling argument dimensionally correct, we write the characteristic time as: $\tau_l = [l/(\delta_l u)]$, where $\delta_l u$ is the characteristic velocity fluctuation at scale l, and an $O(1)$ adimensional constant is absorbed into the characteristic velocity value.

Since the Kolmogorov scaling is observed in the region of wavenumbers $k_c < k < k_\xi$, it exists a corresponding region in real space $\xi < l < l_c$ such that:

$$\frac{\delta_l u^3}{l} = cost$$

which extends down to the healing length. Hence we obtain: $\delta_l u \simeq (\delta_\xi u)(l/\xi)^{1/3}$, for all $\xi < l < l_c$.

Then we can use the experimental values for the typical velocity at the healing length, and the healing length itself: in the experiment H, these are $\delta_\xi u = \xi/\tau_\xi = (0.7 \pm 0.1)\ \mu\mathrm{m\,ps}^{-1}$, where $\xi = (4.6 \pm 0.5)\ \mu$m, and $\tau_\xi = (6.6 \pm 0.7)$ ps.

By applying the τ_l estimate to the scale of the clusters $l_c \simeq 4\xi$, we get: $\tau_{l_c} = [l_c/\delta_{l_c} u] \simeq (16.5 \pm 1.5)$ ps, which tells us that the characteristic time of the clusters at the observed scale l_c is comparable to that observed in the experiments.

Note S8: numerical modelling and simulation results - The collective dynamics of the polariton fluid is described by means of Eq. (1) of the main text, which we solve using a eighth-order Runge-Kutta method on $N^2 = 512^2$ points numerical grid with discretization $a \simeq 0.6\ \mu$m. The turbulent dynamics of the quantum fluid is simulated by starting from a wavefunction with a Gaussian profile (and uniform phase) $\psi(\mathbf{x}, t = 0) = A\exp(-(x^2 + y^2)/2\sigma^2)$ (see Fig. S5a), resembling the resonantly-pulsed excitation applied in the experiments. The parameter $A = \chi n_0^{1/2}$ controls the density of particles (which along

the time evolution is in the order of $|\psi|^2 \sim 10^2$ µm^{-2}), as well as the velocity of the outward particle flux. Therefore, varying the amount of blue-shift in the system corresponds to tuning the parameter χ. For our numerical simulations, we choose the width of the initial Gaussian profile $\sigma = 24.5$ µm, so that the system average healing length is $\xi \sim 2$ µm for $\chi = 0.7$ (n_0 is fixed to 1). A conservative dynamics ($\gamma_c = 0$) is adopted since it has been already successfully employed to simulate quasi-resonant pumping exciton-polaritons [6]. We are careful to simulate the system dynamics in a numerical grid which is at least double the size of the ring diameter, so to avoid artificial boundary effects.

An example of the temporal dynamics from numerical simulations is illustrated by the snapshots in Fig. S5, showing the trapped condensate for $\chi = 0.7$. During the first stage of the dynamics, the condensate radiates isotropically until it hits the hardly-bound confinement, eventually creating density fringes which emerge due to the interference with the reflected wave, Fig. S5b. The wave turbulence is then responsible for the generation a large number of vortices which start to emerge from the centre of the trap (Fig. S5c) and eventually expand throughout the whole sample, where they are free to proliferate (Fig. S5d). The single topological defects is numerically identified computing phase gradients around closed paths of each grid point; more specifically when the circulation around a close path C of double the size of the vortex healing length is found to be approximately 2π [7].

We proceed by investigating the turbulent properties of the fluid at different detuning rates. We explored the dynamics by varying the detunings as $\chi = [0.5; 0.55; 0.6; 0.7]$. Figure S6 shows the physical observables calculated throughout the temporal evolution for L, the lowest detuning (yellow case), and H, the highest detuning (purple case). The quantities are calculated after 100ps, when the vortices have been generated by the initial pulse. In qualitative agreement with the experimental curves reported in the main script (see Fig. 2c and Fig. 3a,b), the numerical curves exhibit an enhanced clustering correlation function (Fig. S6b) for higher detunings. This fact is corroborated by the behaviour of the temporal ratio between incompressible and compressible energies (Fig. S6c) and the fraction between free, dipole and clustered vortices, reported in Fig. S6d and Fig. S6e, respectively. We attribute this feature to stronger interactions between vortices, driven by the mean inter-vortex distance which decreases at higher defect densities. Noteworthy, it is in the late-time dynamics, between 140 and 190 ps, that the system presents the highest number of clustered vortices over dipoles and free vortices, correspondingly to an increment of incompressible

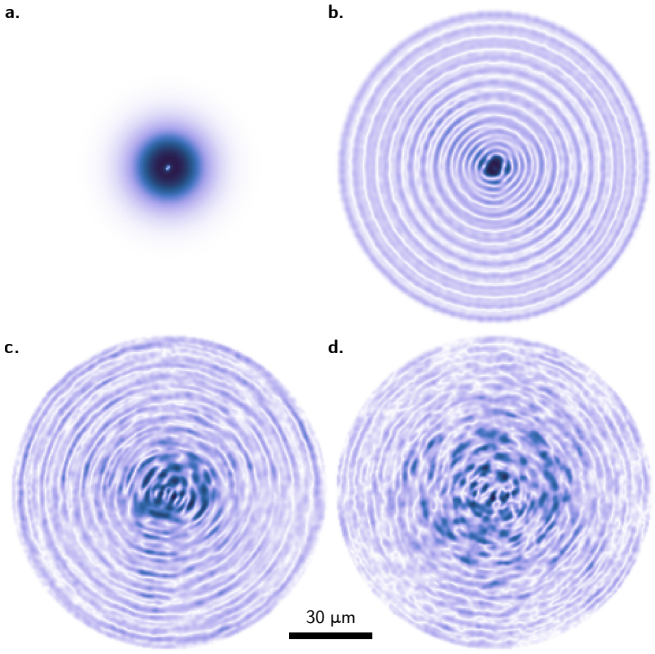

FIG. S5. Temporal evolution of the simulated polariton fluid: the density field within the trap is shown at the starting of the evolution, (a) $t = 0$ when the wavefunction has a Gaussian profile. At intermediate times $t = 70$ ps (b) and $t = 120$ ps (c) the wave-turbulence generates topological defects that at later time $t = 190$ ps (d) proliferate throughout the whole sample.

energy per vortex and highest correlation function values. Finally, adopting the methods explained in Note S4, we compute the incompressible energy spectra for the different cases investigated. Fig. S6f depicts the low- and high-detuned time-averaged spectra calculated in the late-time dynamics of the system. In qualitative agreement with the experimental results shown in Fig. 4a of the main text, the total amount of incompressible energy is found to be larger in the H case when compared to lower detunings. Importantly, the latter case also exhibit the expected scalings for a turbulent quantum fluid [2], in the ranges of wavelength smaller than the inverse of ξ, as well as in the infra-red and ultra-violets part of the spectrum, as discussed in the main paper.

We conclude by discussing the possible role of quantum fluctuations in the turbulent regimes analysed. We perform simulations of the equation of motions for the polariton field $\psi = \psi(\mathbf{r}, t)$ [7, 8] within the Truncated Wigner formulation [8] which reads ($\hbar = 1$):

$$id\psi_c = dt\left[-\frac{\nabla^2}{2m} + g|\psi_c|^2_- + \frac{i}{2}\gamma_c + V(\mathbf{r})\right]\psi_c + dW_c, \tag{S7}$$

where m is the polariton mass, g is the polariton-polariton interaction strength and γ_c

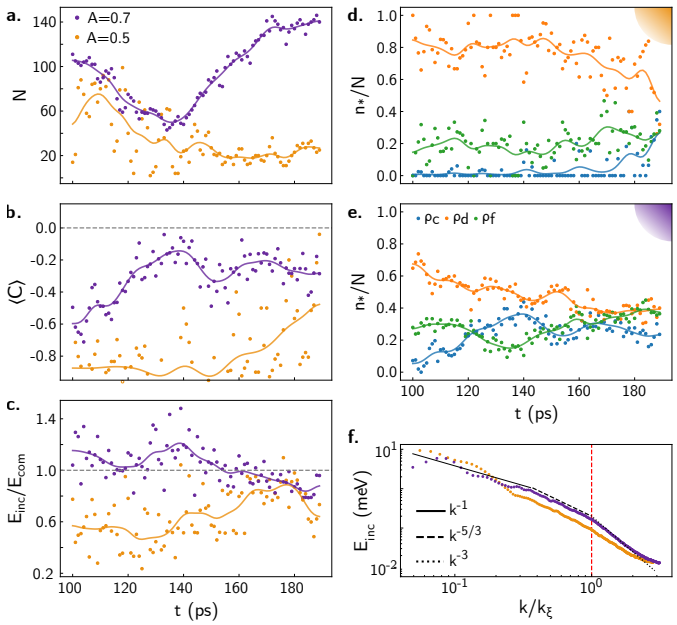

FIG. S6. Physical observables of the system as extracted from the simulations for the lowest and highest detuning value. **a.** Total number of vortices. **b.** Value of the clustering correlation function, which show the increasing trend over time. **c.** Ratio of the incompressible and compressible kinetic energy during the evolution. **d.-e.** Ratios of the number of vortices belonging to clusters (ρ_c), dipoles (ρ_d) or neither of them (free, ρ_f) for the low (d) and high (e) density case, respectively. **f.** Incompressible kinetic energy spectra showing the Kolmogorov scaling in the time range $t \in [140 - 190]$ ps, for wavenumbers smaller than the inverse of the healing length and larger than those dominated by the far-field behaviour.

is the polariton loss rate. Here, $|\psi|^2_-$ corresponds to the renormalized density $|\psi|^2_- \equiv \left(|\psi|^2 - 1/(2dV)\right)$ which includes the subtraction of the Wigner commutator contribution. (Here, $dV = a^2$ corresponds to the volume element of our $2d$ grid of spacing a.) The zero-mean white Wiener noise dW_c fulfils $\langle dW_c(\mathbf{r},t)dW_c(\mathbf{r}',t)\rangle = 0, \langle dW^*(\mathbf{r},t)dW(\mathbf{r}',t)\rangle = \gamma_c/2\delta_{\mathbf{r},\mathbf{r}'}dt$.

We check that simulating with the addition of the stochastic noise do not alter the conclusions presented in this work. This confirms that the turbulent behavior of the system does not arise from the spontaneous formation of vortices due to quantum fluctuations, as seen in previous works [9], but instead takes place at a mean-field level due to the strong wave turbulence generated by the presence of the barrier.

Note S9: results of averaging - To simulate the potential disorder, we add a term $V = d \cdot \varepsilon$ to the dynamic equation

$$i\frac{d}{dt}\psi = H\psi + D \cdot V(x,y)\psi \tag{S8}$$

with ε a real, Gaussian noise distributed in space and constant in time. We vary the real quantity D, while we set $d = 100$ μeV and we add initial random noise to the wavefunction. The effect of disorder on a single shot numerical experiment can be appreciated in the following Fig. S7. We detect the positions of vortices in a time window of 100 ps and, in Fig. S7a, we show the integrated spatial distribution, which confirms that disorder may "localize along set trajectories" vortex cluster generation, suggesting that in the experiment some vortex clusters are not washed out by the randomness of each run [10]. In Fig. S7b, we compare the counts each vortex is detected in a determined spatial position over a period of time of 100 ps. In the presence of disorder, there are more events where some vortex is measured many times in the same grid point, while the histogram is less populated at small vortex counts, accordingly to the physical intuition that hills of potential would generate vortices more frequently in a determined position. In the following, we report the results obtained by numerical simulations of $n = 10$ different stochastic realisations. As shown in the phase profile of the averaged signal in Fig. S8a, vortices mostly remain clear-cut, with a 2π rotation of the phase, confirming that the presence of vortices can be detected from the averaged phase profile at each instant of time. Finally, Fig. S8b shows that by increasing the number of realisations from 3 to 10, one reaches a similar number of vortices to the single-run case in the presence of a moderate level of disorder $D = 0.01$.

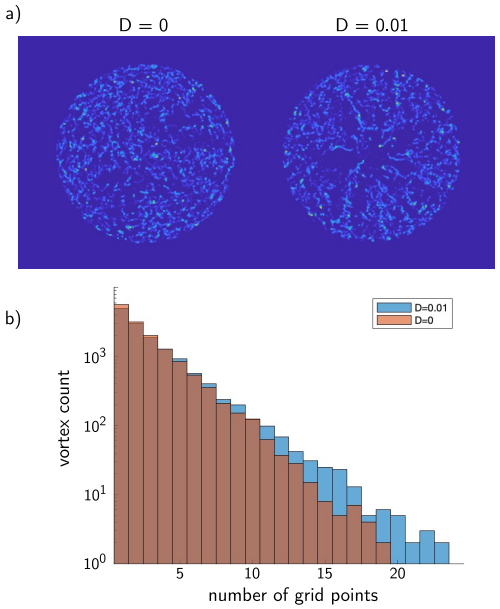

FIG. S7. Effect of disorder on a single shot realisation. **a.**, the spatial distribution of vortices with $D = 0$ (left) and $D = 0.01$ (right) showing the integrated counting of vortices in space between 100 ps and 200 ps. In the case with disorder, the distribution of vortices is less homogeneous, with some regions of the sample where vortices are more often observed. **b.** Comparison of the counts of events in the same spatial position for $D = 0$ and $D = 0.01$. The histogram of the configuration with disorder shows higher frequency for higher vortex counts in the same spatial position.

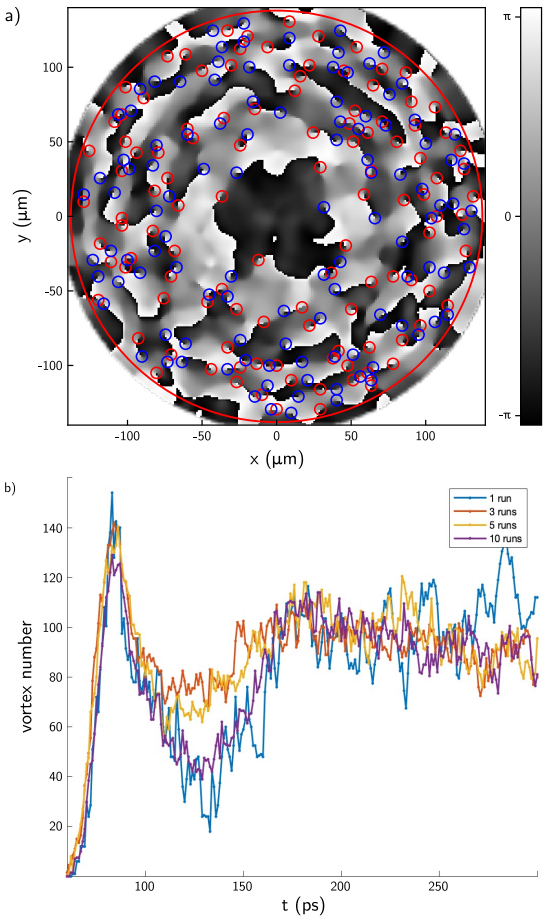

FIG. S8. **a.** Time frame of the phase map, and detection of vortices/antivortices, after averaging 10 stochastic runs, showing that the 2π jumps are preserved. **b.** The number of vortices as a function of time in the presence of a weak disorder $D = 0.01$. The blue curve is a single-shot realisation, other curves are averaging over $n = 3, 5, 10$ stochastic realisations.

[1] C. F. Barenghi and N. G. Parker, *A primer on Quantum Fluids* (Springer, 2016).

[2] A. S. Bradley and B. P. Anderson, Energy spectra of vortex distributions in two-dimensional quantum turbulence, Phys. Rev. X **2**, 041001 (2012).

[3] C. Nore, M. Abid, and M. E. Brachet, Kolmogorov turbulence in low-temperature superflows, Phys. Rev. Lett. **78**, 3896 (1997).

[4] T.-L. Horng, C.-H. Hsueh, S.-W. Su, Y.-M. Kao, and S.-C. Gou, Two-dimensional quantum turbulence in a nonuniform Bose-Einstein condensate, Phys. Rev. A **80**, 023618 (2009).

[5] G. Boffetta and R. E. Ecke, Two-dimensional turbulence, Ann. Rev. Fluid Mech. **44**, 427 (2012).

[6] R. Panico, G. Macorini, L. Dominici, A. Gianfrate, A. Fieramosca, M. De Giorgi, G. Gigli, D. Sanvitto, A. S. Lanotte, and D. Ballarini, Dynamics of a vortex lattice in an expanding polariton quantum fluid, Phys. Rev. Lett. **127**, 047401 (2021).

[7] P. Comaron, I. Carusotto, M. H. Szymańska, and N. P. Proukakis, Non-equilibrium Berezinskii-Kosterlitz-Thouless transition in driven-dissipative condensates (a), EPL (Europhysics Letters) **133**, 17002 (2021).

[8] I. Carusotto and C. Ciuti, Quantum fluids of light, Rev. Mod. Phys. **85**, 299 (2013).

[9] P. Comaron, G. Dagvadorj, A. Zamora, I. Carusotto, N. P. Proukakis, and M. H. Szymańska, Dynamical critical exponents in driven-dissipative quantum systems, Phys. Rev. Lett. **121**, 095302 (2018).

[10] K. Lagoudakis *et al.*, Probing the dynamics of spontaneous quantum vortices in polariton superfluids, Phys. Rev. Lett. **106**, 115301 (2011).